PHYSICAL REVIEW B VOLUME 37, NUMBER 6 15 FEBRUARY 1988-II

X-ray structural study of amorphous Mo-Ge films

J. B. Kortright* and A. Bienenstock
Department of Materials Science and Engineering, Stanford University, Stanford, California 94305

(Received 4 September 1987)

Atomic-scale structural changes with composition in sputtered amorphous Mo-Ge films with compositions from pure Ge to 70 at. % Mo have been studied with radial distribution function (RDF) and differential anomalous scattering techniques, extended x-ray absorption fine structure (EXAFS), and small-angle x-ray scattering. The complementary structural information from large-angle scattering and EXAFS was investigated. The combined techniques indicate that specific chemical ordering between Mo and Ge, much like that in the Ge-rich intermetallic compounds, plays a predominant role in determining the local structures in the Ge-rich amorphous material and continues to play an important role in the Mo-rich material. Three structural regions with composition are distinguished. Structural region I, the semiconductor-metal transition region, extends from *a*-Ge to about 23 at. % Mo. A Mo-modified amorphous structure with distinct local order like that in the Ge-rich compounds coexists with tetrahedral *a*-Ge on a very fine size scale and rapidly modifies the remaining tetrahedral *a*-Ge with continued addition of Mo. All indications of tetrahedral *a*-Ge disappear at about 23 at. % Mo. Region II extends from about 23 to roughly 50 at. % Mo. RDF's and EXAFS show little change with composition in the average structure across this region, which is characterized by strong ordering of Ge about Mo at short distances, long Mo-Mo first-nearest-neighbor distances, and a lack of preferred Ge-Ge distances. The collapse of the long Mo-Mo first-nearest-neighbor distances delimits regions II and III and occurs as the material becomes Mo-rich. At 65 at. % Mo, an RDF and a Mo differential distribution function (DDF) look much like RDF's of typical melt-quenched metal-metalloid glasses. Ge EXAFS and DDF's change little between regions II and III, suggesting that the Mo-Ge interaction persists as the material becomes Mo-rich.

I. INTRODUCTION

Purely amorphous Mo-Ge films can be formed over the composition range from pure Ge to about 75 at. % Mo by co-sputtering the elements onto uncooled substrates. The structures of amorphous Mo-Ge change from open semiconductor to dense, superconducting metal over this unusually broad amorphous composition range. Prior to this work, models existed to describe the amorphous structure at the end points of this composition range, but there had been no determination of how the structure changes across this range.

The structure of pure amorphous Ge (*a*-Ge) is described as a random tetrahedral network (RTN) in which the atoms remain tetrahedrally coordinated, the lack of long-range order resulting from flexibility in bond angles and dihedral angles more than in bond lengths.[1] For the most Mo-rich samples, possible models to describe the structure are those used to describe typical binary transition-metal–metalloid (*T*-*M*) glasses which include, e.g., amorphous Ni-P, Ni-B, Co-P, Au-Si, Pd-Ge, Pt-Si, and Pt-Ge. Common trends among these typical *T*-*M* glasses include their ability to form by melt quenching (and often other techniques) in a narrow composition range around a deep eutectic at about 20 at. % metalloid and, often, a much smaller metalloid than metal atom. The earliest of these models[2] is based on the idea of the smaller metalloid atoms filling larger holes inherent in a dense random packing[3] (DRP) of metal atoms, thus hindering crystallization. The possibility of strong chemical interaction between the metal and metalloid atoms was noted initially,[4] and subsequent discussions often place more emphasis on interaction between species than on size difference and DRP structures.[5,6]

Metal-rich, amorphous Mo-Ge alloys, and closely related amorphous alloys, are very different from the typical *T*-*M* glasses: the equilibrium Mo-Ge system[7] does not have any eutectics; Ge is nearly the same size as Mo; amorphous alloys cannot be melt quenched at room temperature at any composition; and purely amorphous sputtered films cannot be formed on uncooled substrates at the 20 at. % metalloid composition. Binary amorphous systems which share most of these properties with the *a*-Mo-Ge system include Mo-Si,[8] Mo-C,[9] Mo-Al,[8] Nb-Ge,[10] Nb-Si,[10] Cr-Ge,[11] and Cr-Si.[12]

Understanding the structural changes across the amorphous composition range was the primary motivation for this work. A transition from semiconductor to metal occurs rapidly as Mo is added to *a*-Ge.[13] Structural changes accompanying this transition were poorly understood, and of obvious relevance to the changing electrical properties. It had been suggested that, as Mo is added to the *a*-Ge RTN on the 1 at. % level and above, it substitutes for Ge in the RTN,[14,15] or occupies interstitial-like sites in the RTN.[16] With continued addition of Mo to the amorphous films, the extent to which the structures can be described as DRP's of two-size spheres[17] or rather as resulting from specific chemical interaction is of interest. How the amorphous structure at the most Mo-rich compositions compares with that of the typical transition-metal—metalloid glasses was also of interest.

Techniques to study these amorphous structures were chosen both for their ability to provide chemical-specific structural information and to measure interference signals from as wide a region of the spherically symmetric reciprocal space of these samples as possible. These techniques included small-angle x-ray scattering, radial distribution function (RDF) analysis, differential anomalous scattering (DAS),[18] and transmission extended x-ray absorption fine structure (EXAFS).

Until the last decade, direct study of atomic arrangements in binary amorphous samples such as *a*-Mo-Ge relied largely on x-ray or neutron scattering radial distribution functions, and interpretation of the data was often ambiguous because of the inseparability of the signals resulting from the three partial pair correlation functions describing, e.g., the average Ge-Ge, Ge-Mo, and Mo-Mo interatomic correlations. Isotopic substitution and neutron scattering can remove this ambiguity when suitable isotopes exist and when samples large enough for study can be made, neither of which obtain for the thin films studied here and for a wide variety of other materials. DAS and EXAFS use the tunability of synchrotron radiation to at least partially overcome this ambiguity. Amorphous Mo-Ge thin films are well studied for the application of these two species-specific techniques, each of which provides a distorted description of the average environment of a given species. Thus, a secondary motivation for this work was to test the relative amounts of structural information obtained from the species-specific techniques DAS and EXAFS applied to structurally disordered binary alloys.

Small-angle scattering, large-angle scattering (including RDF and DAS techniques), and EXAFS techniques each measure a successively higher region of reciprocal space or momentum transfer, and hence each has a largely different, and complementary, structural sensitivity. Because of its relatively low range in reciprocal space, small-angle scattering (SAS) results from density fluctuations on a size scale larger than interatomic distances. SAS thus helps address the question of compositional inhomogeneity or phase separation which is important over the entire composition range. Large-angle scattering and EXAFS each measure a successively higher region of reciprocal space, each containing signals resulting predominantly from interatomic-scale structure. Because of their largely different ranges, coupled with the large amount of structural disorder in *a*-Mo-Ge alloys (by which is meant a broad range of nearest-neighbor distances on average rather than a single, sharp distribution), EXAFS and large-angle scattering are sensitive to largely different parts of the average near-neighbor environments.[19] Because EXAFS information is not readily interpretable in a large region near the origin of reciprocal space, it is less sensitive to information from all but the sharpest features of the interatomic correlations in these materials.[20] The complementary reciprocal-space ranges of the three techniques together with the species-specific information of EXAFS and DAS provides much direct information on the changing structures with composition.

This paper is organized as follows. Section II describes sample preparation and initial characterization. Section III presents the SAS results. Sections IV and V present the scattering and EXAFS results, with Sec. VI comparing the results of the two techniques. A summary discussion of the structural changes with composition is given in the final section.

II. SAMPLE PREPARATION AND INITIAL CHARACTERIZATION

Thin film samples were prepared by magnetron cosputtering from targets of the elements onto rapidly rotating, uncooled, Kapton substrates using an apparatus described in Ref. 21. The base pressure before deposition was always less than 2×10^{-6} Torr. Purified Ar was used as the sputtering gas at a pressure of 2×10^{-3} Torr. dc and rf power were input into the Mo and Ge targets and varied to control the individual sputtering rates, thus determining the composition. $4\frac{1}{4}$ in. below the targets, 0.003-in.-thick Kapton substrates collected the amorphous deposit. The substrates rotated at about 600 rpm under the two targets, which were tilted to point towards the axis of rotation. Film growth rates ranged from 2 to 4 Å per second. This rotation speed ensured several passes of the substrates for each monolayer of film growth to avoid compositional layering of the films. Total film thicknesses of 3–5 μm resulted from several hours of sputtering. The substrate temperature was not monitored during deposition, and temperatures of 100–200 °C are reasonably expected. Films were prepared on different occasions, always using the same apparatus in the same configuration. No attempt was made to study the effects of varying preparation conditions on the final amorphous structure.

Initial characterization of the films included determination of thickness, using an optical interference microscope, and composition, using an electron microprobe. The compositions quoted as 2 and 4 at. % Mo were obtained by extrapolation of the Mo sputtering rate, because the accuracy of the microprobe (several atomic percent) is limited. Composition was constant within the innermost 2-in. radius of the substrates, and samples for study were taken from their area. The composition measured from both sides of one free-standing film was the same within the measurement error. No Ar was detected in any sample. For several samples, C and O Auger lines were monitored in conjunction with depth profiling by sputtering to learn of the concentrations of these contaminants in the bulk. The intensity of these lines decreased by about 2 orders of magnitude with removal of several hundred angstroms of material. The presence of O and C on as high as the 1 at. % level in the bulk is plausible. No indication of oxide or carbide structures was found in any of the direct structural techniques.

Several layers of Kapton-supported films were typically stacked to provide transmission samples of optimal thickness for the various x-ray techniques.

III. SMALL-ANGLE X-RAY SCATTERING

Small-angle scattering was measured from the amorphous samples to investigate the possibility of compositional inhomogeneity on a larger-than-atomic size scale, which exists over the entire range of compositions studied. High-resolution transmission electron microscopy has provided no indication of phase separation on any size scale across the composition range[22] in the as-deposited films. Thus, any indication of density fluctuations from SAS must either result from extremely small regions or from larger regions with density fluctuations too weak or too few for TEM to observe.

Measurements were made at the SAS beamline 1-4 at the Stanford Synchrotron Radiation Laboratory (SSRL) during dedicated operation of the SPEAR storage ring. The SAS was measured in reciprocal space from $k=0.0064$ to 0.15 Å^{-1} where $k=4\pi\sin(\theta)/\lambda$ is the magnitude of the scattering vector, λ the x-ray wavelength, and 2θ the scattering angle. Details of the experimental apparatus, data reduction to an absolute scale, and interpretation not supplied here can be found in Refs. 23 and 24.

The small-angle x-ray scattering intensity from the amorphous alloys consists of two distinct contributions: a monotonically decreasing intensity localized below 0.05 Å^{-1}, and a roughly constant, diffuse intensity extending across the k range. These two contributions are evident in the data from the 8-at. %-Mo sample in Fig. 1. Based on an independent spherical particle model (Guinier approximation[25]), the SAS localized below 0.05 Å^{-1} results from density fluctuations on a size scale greater than 50 Å and is orders of magnitude too weak to indicate phase separation into well-defined regions of appreciably different density on this size scale. This interpretation holds across the composition range, and is in agreement with TEM images which show no structure on this size scale. The source of this very weak scattering at the lowest k values remains unknown. Possible sources include cracks or internal surfaces, voids, particle inclusions, and surface irregularities.

Of greater relevance to the changing amorphous structure with composition is the weak diffuse intensity which extends across the measured k range with roughly constant intensity as seen in Fig. 1. This diffuse intensity (averaged over the range from 0.05 to 0.15 Å^{-1}) exhibits a trend with composition shown in Fig. 2. The intensity rises quickly from a minimum for a-Ge to a maximum at about 8 at. % Mo and then falls as the Mo content is increased. Interpretation of the fluctuations giving rise to this trend with composition is difficult based on these data alone, and is aided by knowledge of structural results from other techniques presented later. The constant nature of the diffuse SAS with k and its very weak intensity, even when most intense at 8 at. % Mo, suggest that, within the Guinier approximation, very small spheres having relatively little density contrast with a matrix is a reasonable first model to compare with the data. Assuming a 50% by volume mixture of 5-Å-radius spheres in a matrix with a density contrast equal to that between pure a-Ge and that of the amorphous alloy at 25 at. % Mo yields the calculated scattered intensity shown in Fig. 1. (The appropriateness of these densities will become evident in later sections.) The shape profiles do not agree, and even show different trends with k. This is not surprising since the applicability of independent-particle models for such small, densely spaced regions is not expected to be complete. Rather, we would expect inter-region and even interatomic interference effects to be quite strong, leading to a reduction of intensity at the lowest k values compared to that indicated by independent-particle models. The importance of this comparison is that the magnitude of

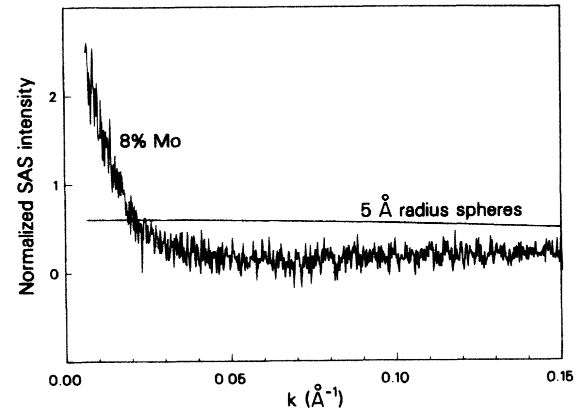

FIG. 1. Normalized small-angle scattering from the 8-at. %-Mo sample shows two distinct contributions, a monotonically decreasing intensity localized below $k=0.05$ Å^{-1}, and a roughly constant diffuse intensity extending across the k range. Data points are connected by a solid line. The smooth curve is a calculation for an independent spherical particle model assuming 5-Å radius spheres comprising 50% by volume with density contrast equal to that for pure a-Ge and the amorphous alloy at 25 at. % Mo.

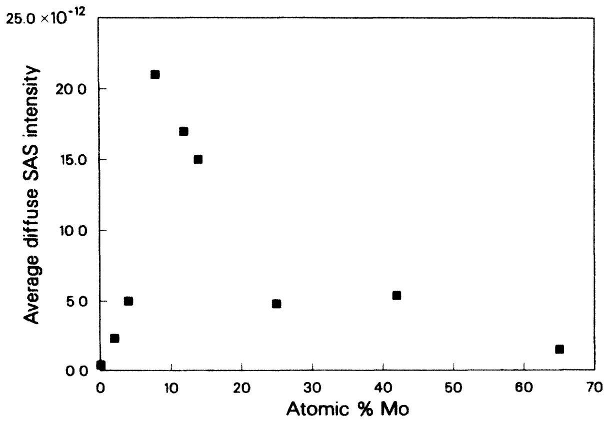

FIG. 2. The average of the diffuse SAS intensity seen in Fig. 1 for the 8-at. %-Mo sample is plotted here for a range of compositions. The trend with composition interpreted as reflecting a maximum inhomogeneity at roughly 8 at. % Mo existing on a size scale of order 10 Å.

the diffuse intensity is not far from that calculated for a model based on phases that are dispersed on a very small size scale with reasonable density differences. Model calculations assuming larger particles with similar volume fractions and density contrasts indicate intensity localized toward lower k values with orders greater intensity, and are not consistent with the data or the TEM results.

From the trend in the SAS in Fig. 2, together with these comparisons with simple models, we infer that some inhomogeneity does exist as Mo is added to a-Ge, and that this inhomogeneity is present on a very fine size scale of the order of 10 Å. Neither SAS nor TEM are consistent with large density fluctuations on size scales larger than this. The maximum in the diffuse SAS intensity at about 8 at. % Mo suggests that the inhomogeneity is a maximum at this composition, and that it decreases rapidly as more Mo is added to a-Ge. Large-angle scattering and EXAFS results in the following sections are consistent with this interpretation of inhomogeneity on a very fine size scale, and yield much information about the atomic-scale structure of the regions making up this inhomogeneity.

IV. LARGE-ANGLE SCATTERING RESULTS

Large-angle scattering measurements were made using the materials diffractometer on the wiggler beamline 4-3 during dedicated operation at SSRL. The room-temperature samples typically consisted of two or three layers of Kapton-supported films held flat on the axis of the diffractometer by a metal frame in a symmetric transmission geometry. The scattered intensity was measured in step-scan fashion by a scintillator crystal (NaI) and photomultiplier detector. This detector's poor energy resolution meant that it counted any sample fluorescence from the species near whose absorption edge the incident energy was tuned. Solid-state detectors capable of measurement in the vertical plane are now used for this experiment, and discriminate against the $K\alpha$, but not the $K\beta$ fluorescence and much of the Compton scattering.

Accurate knowledge of the changing anomalous scattering factors (ASF) with energy is essential to obtain reliable information from anomalous scattering techniques. The atomic scattering factor is given by $f(k,E)=f_0(k)+f'(k,E)+if''(k,E)$ where E is the photon energy. $f_0(k)$ is the energy-independent form factor, whose values for this work were taken as those calculated for isolated atoms,[26] and describes the scattering amplitude in the high-E limit. The ASF $f'(k,E)$ and $f''(k,E)$ are quite appreciable when photon energies are near absorption edges. f'' is directly proportional to absorption coefficient, and was obtained from absorption data taken for the EXAFS experiment which had been fit to published values[27] far from each species' K edge to obtain an absolute scale. f' was obtained from f'' by the Kramers-Kronig dispersion relation.[28] The ASF thus obtained agree very well the calculated free-atom values[29] except very near to and above the absorption edges, where solid-state effects introduce structure not present in the calculated, free-atom ASF.

Normalization of each data set to an absolute, per atom scale involved subtraction of the correctly attenuated Kapton substrate intensity, determination of the amount of fluorescence in the data and its subtraction, subtraction of the calculated Compton intensity, determination of the scaling constant for the coherent intensity, and correction for distortions of each of these signals due to the changing sample size and absorption with θ resulting from the transmission geometry used. Corrections for these distortions require knowledge of the absorption products $\mu t(\theta)$ at various energies, which were measured under the same experimental conditions for which the data were collected. Two adjustable parameters were employed in the normalization of each data set, the average density of the sample and a single $\mu t(\theta)$ value used to describe the combined absorption of both $K\alpha$ and $K\beta$ fluorescence. Details of the normalization are found in Refs. 24 and 18.

A. RDF results

For a single incident photon energy the intensity coherently scattered by the binary a-Mo-Ge samples can be expressed by a sum of three species-specific contributions as

$$\begin{aligned} I(k,E) = {} & w_{\mathrm{GeGe}}(k,E)[S_{\mathrm{GeGe}}(k)+1] \\ & + w_{\mathrm{GeMo}}(k,E)S_{\mathrm{GeMo}}(k) \\ & + w_{\mathrm{MoMo}}(k,E)[S_{\mathrm{MoMo}}(k)+1] \; . \end{aligned}$$

Here

$$w_{\mathrm{GeGe}}(k,E)=x_{\mathrm{Ge}}f^{*}_{\mathrm{Ge}}(k,E)f_{\mathrm{Ge}}(k,E)$$

and

$$w_{\mathrm{GeMo}}(k,E)=2x_{\mathrm{Ge}}\mathrm{Re}[f^{*}_{\mathrm{Ge}}(k,E)f_{\mathrm{Mo}}(k,E)]$$

are structure-independent weighting factors, x_{Ge} is the atomic fraction of Ge, and $S_{\mathrm{GeGe}}(k)$ is the partial structure factor describing the k-space interference oscillations resulting from the Ge-Ge atomic correlations. A total structure factor $S(k)$ is obtained from this intensity and is related to the deviation from the average number density of atoms[30] by

$$\begin{aligned} S(k) & = [I(k)-\langle f^2\rangle]/\langle f\rangle^2 \\ & = (1/2\pi)\int r[\rho(r)-\rho_{\mathrm{av}}]\sin(kr)dr \; . \end{aligned}$$

Real-space information $r[\rho(r)-\rho_{\mathrm{av}}]$ is obtained from the inverse transform, and the RDF is $4\pi r^2\rho(r)$. The RDF gives a weighted sum of all three partial distribution functions and, hence, is somewhat ambiguous.

$S(k)$'s and RDF's for a series of compositions ranging from a-Ge to 65 at. % Mo are shown in Fig. 3 and are obtained using a photon energy 500 eV below the Mo K edge. The RDF's are of high quality, as evidenced by the lack of spurious oscillations at distances below the first peak. The average density, ρ_{av} was systematically varied in the normalization of the data to obtain these RDF's. The best ρ_{av} values were determined as those which yielded the flattest low-r behavior in the resultant

RDF's, and are estimated accurate to ±0.2 g/cm^3. The resultant best apparent densities are in Table I as are the first peak positions and areas. Areas were measured out to the minimum between the first and second peak.

Gross changes in the average structure with composition are seen in Fig. 3. Three structural regions, each existing over a range of compositions, can be distinguished from both the $S(k)$'s and the RDF's. Region I extends from *a*-Ge to somewhat less than 25 at. % Mo. Over this composition range all traces of the *a*-Ge RTN disappear, as evidenced by the disappearance both of the distinctive pattern of the *a*-Ge $S(k)$ and of features in the RDF's at the positions of the three peaks in the *a*-Ge RDF. The *a*-Ge RTN is replaced by an average structure with larger average coordination number and longer near-neighbor distances, signaling the transition from semiconductor to metal. Accompanying the disappearance of the *a*-Ge RTN is an increase in the first peak area, even at only 2 and 4 at. % Mo, which is sufficiently rapid that it indicates that Mo does not substitute for Ge in the RTN, but rather increases the average coordination.

Region II extends from somewhat less than 25 at. % Mo to somewhere between 42 and 65 at. % Mo. No clear indication of the *a*-Ge RTN is evident in the RDF's or $S(k)$'s here, and even at 25 at. % Mo the first shell average coordination of 12 is indicative of a metallic structure. The average structure changes little with composition between 25 and 42 at. % Mo and appears to have poorly defined average coordination shells, as seen by the shallow minimum in the RDF's between the first and second peaks.

Large structural changes are seen on going to the Mo-rich end of the composition range, which comprises structural region III. At 65 at. % Mo the RDF and $S(k)$ look much like those of typical melt-quenched metallic glasses,[31] with a large, well-defined first peak and a split second peak in both k and r space.

The changing structure through the semiconductor-metal transition region I is of special interest, and an apparent mixture of *a*-Ge and a Mo-modified structure through this transition lends an interpretation to the SAS trends which suggest a maximum inhomogeneity in this region. With the lack of *a*-Ge features at 25 at. % Mo, the similar features of the 25 and 42 at. % Mo RDF's and the appearance of these features at less than 25 at. % Mo, it is reasonable to hypothesize that the emerging Mo-modified structure is described by the structure at 25 at. % Mo. If, at intermediate compositions, the amorphous structure is a mixture of large, well-defined regions of *a*-Ge and the modified 25-at. %-Mo structure, then the actual $S(k)$ would approach a superposition of appropriate amounts of the *a*-Ge and 25 at. % Mo $S(k)$'s.

Superpositions in proportion to composition of the *a*-Ge and 25 at. % Mo $S(k)$'s are compared with the actual $S(k)$'s at 8 and 14 at. % Mo in Fig. 4. Strong similarity of the two signals at each composition is seen, though differences are apparent out to at least 6.0 Å^{-1}. The strong interference peaks of the actual $S(k)$'s do contain features at k values closely corresponding to those in the

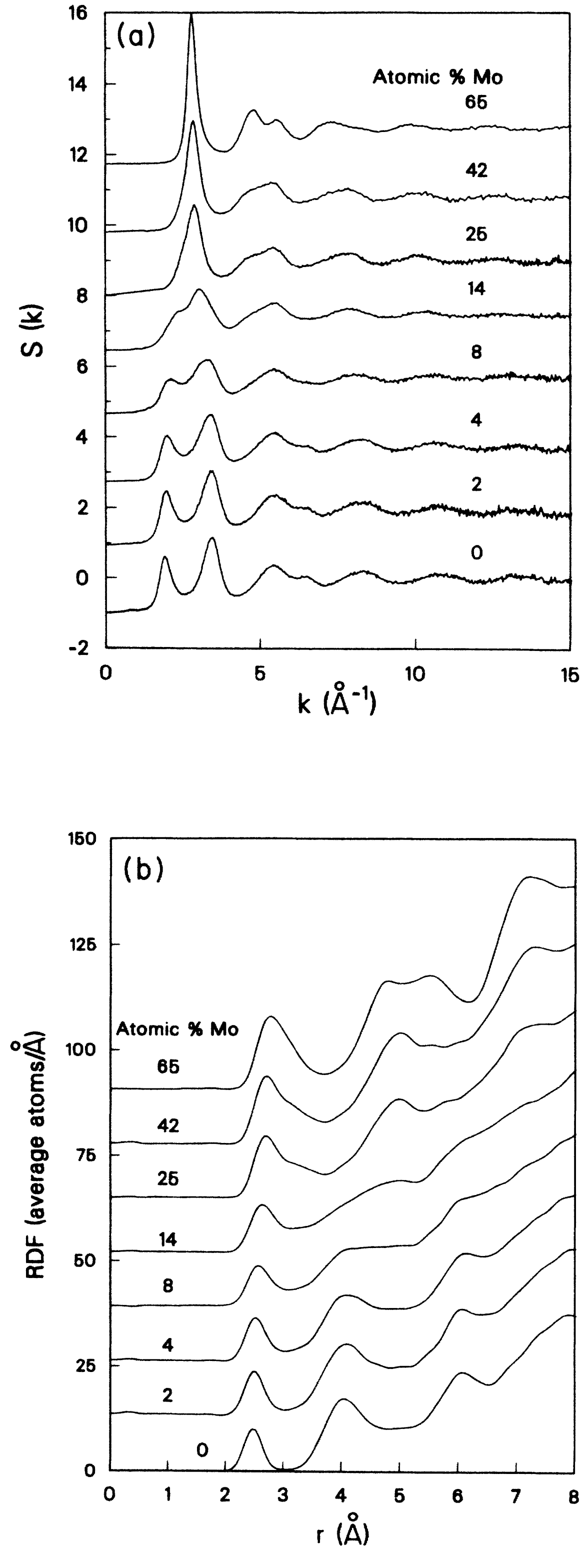

FIG. 3. Total structure factors $S(k)$'s are shown in (a) for a series of *a*-Mo-Ge samples with compositions as noted. All data were collected with photon energy either 400 or 500 eV below the Mo K edge (19 999 eV), and are plotted on the same scale but offset vertically for comparison. In (b) are the corresponding RDF's.

TABLE I. RDF results.

Mo concentration (at. %)	Density (g/cm^3)	Position (Å)	Peak area[a]	
0	5.3	2.47	4.0	
2	5.7	2.48	4.4	
4	5.9	2.49	4.8	
8	6.3	2.54	5.2	
14	6.8	2.60	6.0	10.4
25	7.4	2.67		12.3
42	7.8	2.67		12.4
65	9.3	2.74		13.5

[a]Areas represent a compositionally averaged number of atoms because of the normalization used and can be converted into units of (electron)^2. Areas were measured from 2.0 Å to the minimum between the first and second peaks. For the left column this minimum was about 3.0 Å while for the right column it was about 3.7 Å. See Ref. 24 for more details.

superposed $S(k)$'s, but smeared in such a way that they appear at k values intermediate between those of the superposed signals. This suggests that the average structure at 8 and 14 at. % Mo does contain regions with local structure like a-Ge and the 25-at. %-Mo structure, and that interference between the signals from these regions may account for the differences between the actual and superposed $S(k)$'s. This is less consistent with phase separation into large regions of these two local structures, where this inter-region interference would not be as strong, and is more consistent with mixing of these two local structures on a fine size scale. The same conclusion would be obtained using the 42 at. % Mo $S(k)$ to represent the Mo-modified material coexisting with the tetrahedral Ge in this superposition, because of the similarity of the $S(k)$'s at 25 and 42 at. % Mo.

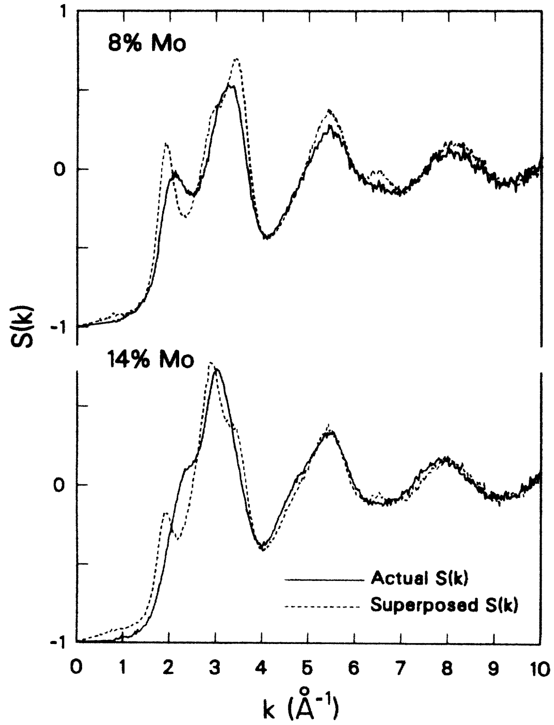

FIG. 4. Total structure factors $S(k)$ are shown for the 8- and 14-at. %-Mo a-Mo-Ge samples as solid lines. The dashed lines are superpositions in proportion to composition of the a-Ge and 25 at. % Mo $S(k)$'s, and show that the actual structure at these compositions does have features similar to the a-Ge and 25-at. %-Mo structures.

RDF's and $S(k)$'s tell much about the average structure at a given composition and its change with composition. They show the replacement of the a-Ge RTN by a distinct Mo-modified amorphous structure by 25 at. % Mo signaling the semiconductor-metal transition (region I). In region II the average structure appears to change little with composition, and appears to be much like that of the emerging Mo-modified material of region I. In region III, the average structure shows features typical of common metal-metalloid glasses and other metallic glasses often described by DRP models. RDF's do not, however, provide any direct information about differences in the average environment about each species at a given composition. Hence the motivation for application of species-specific anomalous scattering and EXAFS techniques.

B. Differential anomalous scattering results

The DAS technique[18] uses two independent data sets collected using two incident photon energies near a given species' absorption edge, where only that species' ASF are changing rapidly with energy. DAS analysis begins by subtracting the self-scattering from each of the two normalized data sets to give $I(k)-\langle f^2\rangle$. If the two photon energies are close to the Ge K edge, and letting $\Delta_{\rm Ge}[\;]$ represent the difference with energy of the quantity in brackets, then the difference of the two reduced intensities is

$$\Delta_{\rm Ge}[I(k,E)-\langle f^2\rangle]=\Delta_{\rm Ge}[w_{\rm GeGe}(k,E)]S_{\rm GeGe}(k)+\Delta_{\rm Ge}[w_{\rm GeMo}(k,E)]S_{\rm GeMo}(k)\;.$$

Similar to the RDF case, the k dependence of the weighting factors is approximately removed and the data put on a per atom scale by dividing by

$$W(k,E_1,E_2)=\Delta_{\rm Ge}[w_{\rm GeGe}(k,E)]+\Delta_{\rm Ge}[w_{\rm GeMo}(k,E)]$$

to yield a differential structure factor $\Delta_{\rm Ge}[S(k)]$, which now contains information about Ge-Ge and Ge-Mo correlations but not Mo-Mo correlations, since the Mo ASF are, to a good approximation, constant at the two energies used in the difference. The sine transform of $\Delta_{\rm Ge}[S(k)]$ yields a weighted sum of the quantity $r[\rho_{\rm GeGe}(r)-\rho_{\rm Ge\;av}]+r[\rho_{\rm GeMo}(r)-\rho_{\rm Mo\;av}]$, to which $r\rho_{\rm av}$ is added and the result weighted by r to give the Ge differential distribution function (DDF). The DDF shows the average environment about just Ge atoms, and, hence, is less ambiguous than the RDF. The same procedure using two data sets taken with photon energies near the Mo K edge yields a Mo DDF.

Ge and Mo DDF's were obtained using data sets taken with photon energies immediately and farther below each species' K edge for compositions of 14, 42, and 65 at. % Mo. Table II shows the photon energies and asso-

TABLE II. Anomalous scattering factors for DAS technique. Photon energies are measured relative to the K edge of the species whose edge is being utilized for the DAS effect.

	Energy (eV)	Mo f'	Mo f''	Ge f'	Ge f''
			14-at.%-Mo sample		
Ge DAS	-200	-0.6	1.6	-3.5	0.5
	-25	-0.6	1.6	-6.1	0.6
Mo DAS	-500	-3.3	0.5	0.2	1.5
	-10	-7.7	1.0	0.2	1.5
			42-at.%-Mo sample		
Ge DAS	-200	-0.6	1.6	-3.5	0.5
	-15	-0.6	1.6	-7.0	0.7
Mo DAS	-400	-3.5	0.5	0.2	1.5
	-12	-7.3	1.0	0.2	1.5
			65-at.%-Mo sample		
Ge DAS	-200	-0.6	1.6	-4.0	0.5
	-5	-0.6	1.6	-11.5	0.8
Mo DAS	-400	-3.5	0.5	0.2	1.5
	-30	-6.5	0.6	0.2	1.5

ciated anomalous scattering factors used in obtaining these DDF's. Figures 5 and 6 show $\Delta[S(k)]$'s and DDF's for Ge and Mo, respectively, indicating how the Ge and Mo average environments change with composition. In Fig. 5, the *a*-Ge total $S(k)$ and RDF are included for comparison. First-peak positions and areas are presented in Table III, with the areas again measured to the minimum between the first and second peaks. In Fig. 7 the Ge and Mo DDF's at each composition are superimposed. Recalling that Ge DDF's contain only Ge-Ge and Ge-Mo correlations while Mo DDF's contain only Mo-Mo and Mo-Ge correlations allows us to infer much from Fig. 7 about how the three individual pair correlations contribute to the DDF's.

At 14 at. % Mo (in region I) the average Ge and Mo environments are very different. The Ge environment is quite disordered on average, as seen by the poorly defined first shell with many apparent distances between the first and second peaks, and broad, almost featureless second and higher shells. Some tetrahedral *a*-Ge is still present as indicated by slight shoulders at the second and third *a*-Ge peak distances. The disordered part of the Ge environment comes from modification by Mo. The average first-shell coordination number is still rather small, with the increase due largely to increasing coordination at longer distances. The first peak is at 2.65 Å, about 0.2 Å longer than the Ge-Ge distance in *a*-Ge. The Mo average environment at 14 at. % Mo has a relatively well-defined first shell composed of a major peak at about 2.7 Å and a small shoulder at about 3.3 Å. No indication of tetrahedral *a*-Ge structure is present in the Mo DDF: the first-peak area is not consistent with Mo substitutional in the *a*-Ge RTN and the shoulder has no counterpart in the tetrahedral bonding scheme. Rather, Mo is associated with a modified structure.

At 42 at. % Mo (in region II) no signs of the *a*-Ge RTN are present in the Ge DDF. The Ge first-shell coordination has increased to roughly equal that of Mo, and the overall Ge DDF profile has changed markedly from that at 14 at. % Mo. The Ge DDF continues to show broader, less well-defined average coordination shells than the Mo DDF, and a value well above zero between the first and second peaks. The Mo DDF changes much less than the Ge DDF on going from 14 to 42 at. % Mo, the major change being an increase in

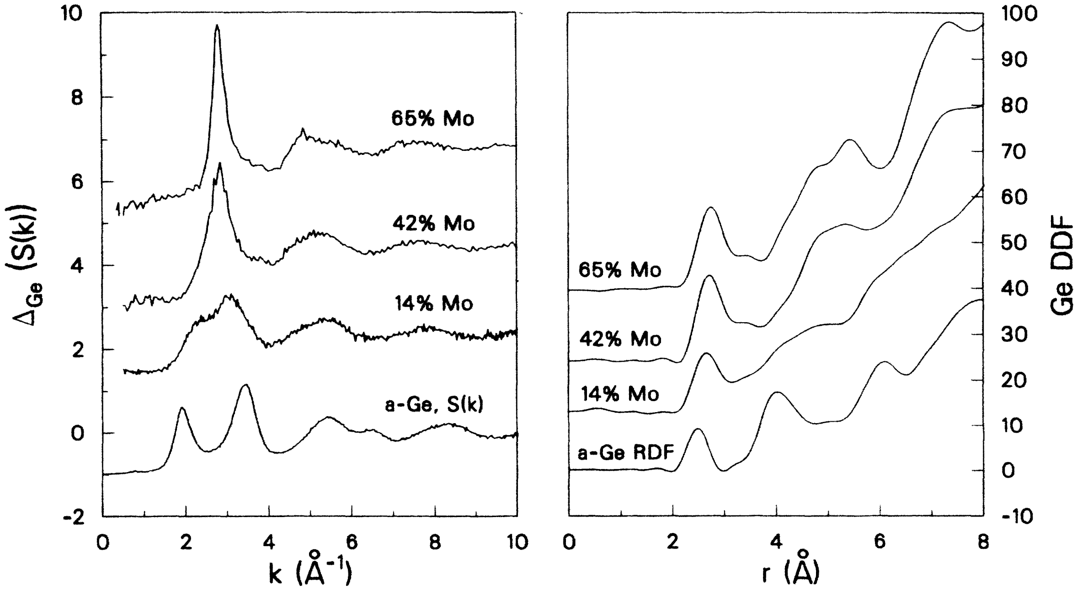

FIG. 5. Ge differential structure factors $\Delta_{Ge}[S(k)]$ and corresponding DDF's are shown for *a*-Mo-Ge samples with compositions 14, 42, and 65 at. % Mo. For *a*-Ge, $S(k)$ and the RDF are shown for comparison. All data are plotted on the same scale and offset for comparison.

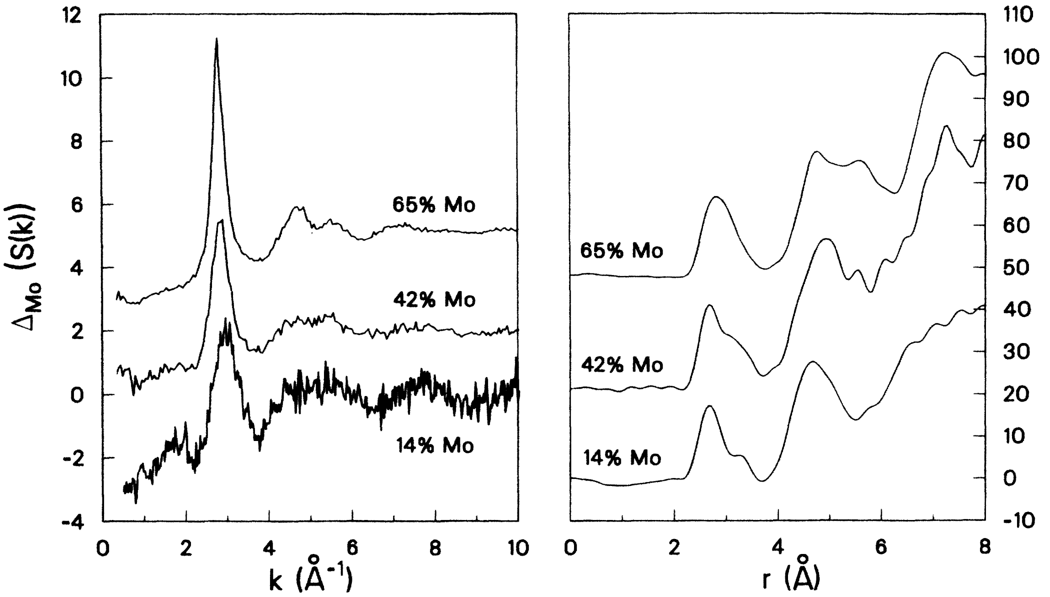

FIG. 6. Mo differential structure factors $\Delta_{Mo}[S(k)]$ and corresponding Mo DDF's are shown for *a*-Mo-Ge samples with composition 14, 42, and 65 at. % Mo. All data are plotted on the same scale and offset for comparison.

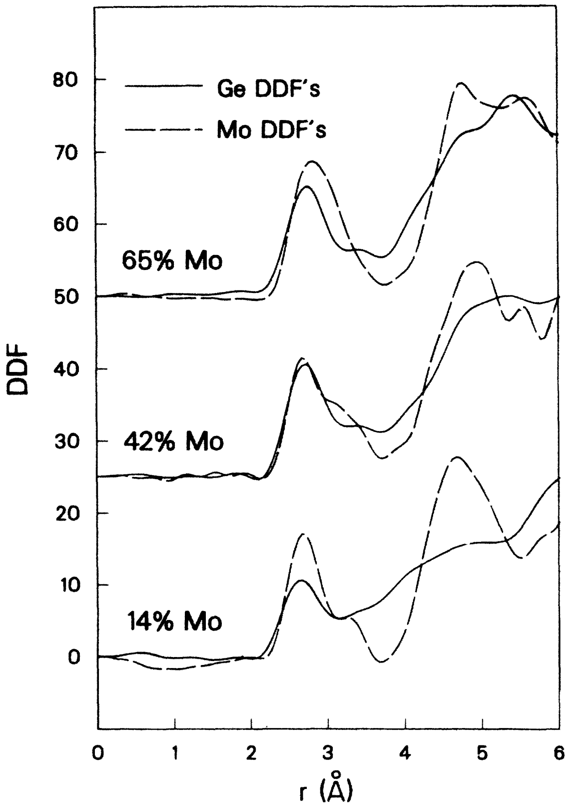

FIG. 7. DDF's for a given composition are superimposed here, and different compositions are plotted on the same scale but offset vertically. Plotted this way, much can be inferred about how the three pair correlations contribute to the average structure at each composition and how these contributions change with composition.

the shoulder on the high-*r* side of the first peak. The identical first part of the first peaks of the Mo and Ge DDF's at 42 at. % Mo (see Fig. 7) is direct evidence that this is a Mo-Ge feature. This same feature in the Mo DDF at 14 at. % Mo suggests that this too is a Mo-Ge feature. The shoulder at roughly 3.3 Å on the high-*r* side of the Mo DDF first peak at 42 at. % Mo does not have a counterpart in the Ge DDF (see Fig. 7), identifying this as a Mo-Mo feature. Likewise this emerging feature at 14 at. % Mo is also a Mo-Mo feature. The large amount of disorder between the first and second peaks in the Ge DDF's at both 14 and 42 at. % Mo have no counterpart in the Mo DDF's, so that this structural disorder not only exists primarily around Ge but results primarily from Ge-Ge correlations. All of these identifications of individual pair correlations (Mo-Ge shortest, Mo-Mo quite long, and Ge-Ge relatively disordered) are very similar to those in both of the Ge-rich intermetallic compounds Ge_2Mo and $Mo_{13}Ge_{23}$.[19]

At 65 at. % Mo (in region III) the Ge DDF is very

TABLE III. DAS results.

Mo concentration (at. %)	Peak position (Å)	Peak area[a]	
	Ge DDF's		
14	2.65	6.5	
42	2.71	9.0	13.7
65	2.74	9.5	13.0
	Mo DDF's		
14	2.68	8.6	10.5
42	2.69	8.7	12.7
65	2.81		14.3

[a] Peak areas approximate a compositionally average number of atoms and are measured from 2.1 to 3.1 or 3.8 Å for the values found in the first and second columns.

similar to that at 42 at. % Mo but the Mo DDF is very different from that at 42 at. % Mo. The Mo-Ge main peak of the Ge DDF remains constant in size and position between 42 and 65 at. % Mo, as does the disorder between the first and second peaks. The Mo DDF shows that the long Mo-Mo first distance seen at 42 at. % Mo has collapsed to lower r into a very broad first shell at 65 at. % Mo. Given that the short Mo-Ge distances remain intact, as seen from the Ge DDF, the shorter Mo-Mo distances at 65 at. % Mo must still be predominantly on the far side of the Mo DDF first peak. The Mo DDF and Mo $\Delta[S(k)]$ at 65 at. % Mo look much like RDF's and $S(k)$'s of typical melt-quenched T-M glasses.[31]

The presence of Mo-Mo correlations at about 3.3 Å at 14 at. % Mo in the Mo DDF has implications regarding the homogeneity of the material at this composition. Given the average density of about 6.8 g/cm^3 and the composition, the average number density of Mo atoms is calculated to be 0.0076 Å^{-3}, implying an average linear separation between Mo atoms of 5.1 Å, assuming they are dispersed on a simple cubic lattice. The fact that Mo-Mo correlations are seen at about 3.3 Å may be evidence that some segregation of Mo atoms is occurring at this composition. This short observed Mo-Mo distance in itself says nothing about the size scale of the segregation of Mo atoms into regions with local structure like that of the Ge-rich compounds. Evidence that the size scale of these Mo-modified regions at 14 at. % Mo is small comes from comparison of the intensity of the Mo-Mo shoulder of the 14 at. % Mo DDF with the same feature at 42 at. % Mo. At 42 at. % Mo this Mo-Mo shoulder has roughly the same area as it would for the Ge-rich crystals,[24] while at 14 at. % Mo this area is much smaller. This is more consistent with the Mo-modified regions existing with a very high surface-to-volume ratio (i.e., very dispersed) rather than in large, well-defined regions. Indeed, the difference between the homogeneously dispersed distance and the observed shorter distance is less than an atom spacing, so that diffusion of only a very short distance is required for this segregation. This interpretation of a finely dispersed mixture is also consistent with the interpretation of Fig. 4 and with SAS and TEM results.

In summary, the DDF's reveal much species-specific information that the RDF's cannot provide. At 14 at. % Mo the Ge DDF shows indication of the a-Ge RTN and much disorder, which results from modification by Mo. Mo has a more ordered environment than does Ge, with a first peak due mainly to Mo-Ge correlations and a small contribution at larger r due to Mo-Mo correlations. The DDF's show the major change between regions I and II to be the disappearance of the a-Ge RTN. In region II the average structure is characterized by short Mo-Ge correlations, long Mo-Mo correlations, and disordered Ge-Ge correlations, much like in the Ge-rich compounds. The major change between regions II and III is the collapse of the long Mo-Mo correlations from about 3.3 Å to shorter distances in the first shell, but still longer than the Mo-Ge distances which appear to remain unchanged from region II. In region III the average structure looks much like that of metallic glasses described by DRP models, and Mo-Mo correlations predominate in this appearance. Similarities and differences between Mo and Ge DDF's allow identification of how the individual pair correlation functions contribute to the structure.

V. EXAFS RESULTS

Absorption data were collected from many samples ranging in composition from a-Ge to 70 at. % Mo above the Mo and Ge K edges on several occasions at SSRL beamlines 1-5 and 4-2 during both parasitic and dedicated operation of the SPEAR storage ring. The same apparatus in the same configuration was always used, and consisted of $6\frac{3}{4}$- and $12\frac{3}{4}$-in. ion chambers before and behind the samples, filled with N_2 and Ar slightly above atmospheric pressure when working near the Ge and Mo edges, respectively. The samples were held in transmission geometry near 77 K in an evacuated Dewar with Kapton windows. The incident beam monochromator was typically detuned about 30% to minimize harmonic contamination of the beam. The EXAFS signal, $\chi(k)$, was obtained and normalized using standard procedures.[24]

Structural information was obtained primarily from modeling the data in k space, and also by observing trends in the data with composition. In modeling, the $k^3\chi(k)$ were assumed to conform to the expression

$$k^3\chi_\alpha(k)=k^2\sum_\beta \frac{N_\beta}{R^2_{\alpha\beta}}\exp(-2\sigma^2_{\alpha\beta}k^2)\,|f_\beta(\pi,k)| \times\sin[2kR_{\alpha\beta}+\phi_{\alpha\beta}(k)]\ . \qquad (1)$$

Here, α refers to the absorbing atom species and β to the backscattering atoms a distance $R_{\alpha\beta}$ from the absorbing atom. N_β gives the effective number of atoms of a given species at a given distance and $\sigma^2_{\alpha\beta}$ is a description of Gaussian static and thermal broadening of that shell. $f_\beta(\pi,k)$ is the backscattering amplitude and $\phi_{\alpha\beta}(k)$ gives the combined phase shift experienced by the photoelectron on ejection from the absorbing atom, backscattering, and return to the absorbing atom. Calculated values of $f_\beta(\pi,k)$ and $\phi_{\alpha\beta}(k)$ (Ref. 32) were used in the modeling because the structures of the Mo-Ge compounds are not simple enough to determine these quantities in all possible cases. When possible, these calculated values were checked by modeling the EXAFS from standards with simple enough structures, and were found to give good agreement with the observed data.[24] Absent from this expression for the EXAFS are factors accounting for mean-free-path and many-body effects, which represent alternative channels for the photoelectrons and, hence, reduce the magnitude of the EXAFS effect. These effects are not well characterized theoretically, and are essentially constant for a given shell. Empirical backscattering amplitudes would include these effects, at least approximately, but the calculated amplitudes used here do not take them into account. They are implicitly included in N_β, which is thus expected to have a smaller value than the actual coordination number. Possible multiple-scattering effects[33,34] are also neglected.

One- and two-shell modeling used a nonlinear least-squares fit of Eq. (1) to the data in which R, N, and σ^2 for each shell were varied as parameters of the fit. Backscattering phase shifts of Mo and Ge differ by about 2 rad over most of the k range, thus facilitating identification of backscattering species in modeling of EXAFS from the amorphous alloys. Models with more than two shells were not investigated because the data were typically well fit with only one or two shells, and because of the rapid proliferation of variable parameters. The zero of the photoelectron energy scale, E_0, was not varied in the fit itself, but rather we investigated the sensitivity of the fit results to different, fixed values of E_0. In general, modeling trends are independent of E_0, though parameters of the fits undergo small systematic changes with E_0. Before modeling, the data were windowed by a Gaussian broadened square window from 3.0 to 15.0 Å^{-1} for Ge EXAFS and from 4.0 to 12.0 Å^{-1} for Mo EXAFS. The same windows were incorporated into the models. Because the calculated $f_\beta(\pi,k)$ and $\phi_{\alpha\beta}(k)$ are available for $k > 3.8$ Å^{-1}, modeling began at that k value. A goodness of fit parameter, Σ, defined here as the sum of squares of the residuals between the model and data at the data points divided by the sum of squares of the data points, is useful in comparing different models for a given data set.

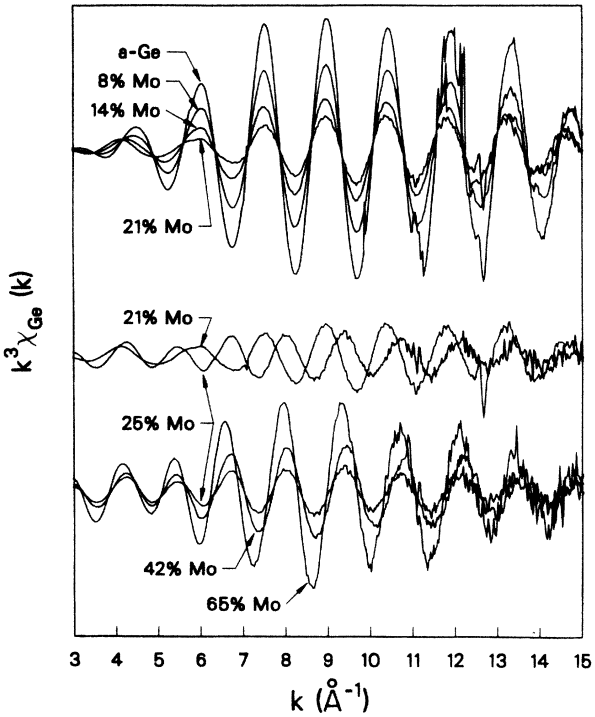

FIG. 8. Ge $k^3\chi(k)$ for a series of a-Mo-Ge samples with compositions from a-Ge to 65 at. % Mo are shown here, all plotted on the same vertical scale but offset vertically for comparison.

A. Ge EXAFS modeling results

EXAFS signals $k^3\chi_{Ge}(k)$ from above the Ge K edge are shown in Fig. 8 for samples with compositions from a-Ge to 65 at. % Mo. Strong trends with composition are seen. For 21 at. % Mo and less, the EXAFS shows primarily the same phase but with decreasing amplitude with increasing Mo content. A distinct change in phase occurs between 21 and 25 at. % Mo, and for convenience we take 23 at. % Mo as the composite delimiting this change. This change coincides with the distinction of regions I and II identified from the scattering results, reinforcing the interpretation that major changes in the average Ge environment delimit regions I and II. With increasing Mo content from 25 at. % Mo, the phase and amplitude profile change little while the amplitude increases. Modeling results are discussed for the composition ranges less and greater than 23 at. % Mo in turn.

In the range from a-Ge to 23 at. % Mo, the EXAFS data can be well fit with a Ge one-shell model at the tetrahedral distance, and at 14 and 21 at. % Mo with two-shell models with both Ge and Mo shells. Table IV shows the parameters returned from the fits, which are superimposed on the data in Fig. 9. The effective coordination number of Ge about Ge in pure a-Ge is 2.8 instead of the known value of 4, reflecting the neglect of non-EXAFS effects and, perhaps, errors in the calculat-

TABLE IV. Ge EXAFS modeling results (≤ 21 at. % Mo). The E_0 used to obtain these results is that used to make $k^3\chi(k)$ for a-Ge give the tetrahedral distance (2.45 Å) and is located about 6 eV above the peak of the resonant line near the Ge K absorption edge.

Mo conc.	Ge shell			Mo shell			
(at. %)	R	N	σ^2	R	N	σ^2	Σ
			One-Ge-shell results				
0	2.45	2.80	0.0031				0.038
8	2.45	1.88	0.0039				0.011
14	2.46	1.07	0.0032				0.035
21	2.46	0.52	0.0018				0.036
			Two-shell results				
0	2.45	3.26	0.0036	2.56	0.17	0.0006	0.036
8	2.45	1.74	0.0033	2.61	24.1	0.105	0.020
14	2.46	1.20	0.0037	2.61	1.00	0.0167	0.033
21	2.46	0.60	0.0023	2.62	1.10	0.0169	0.057

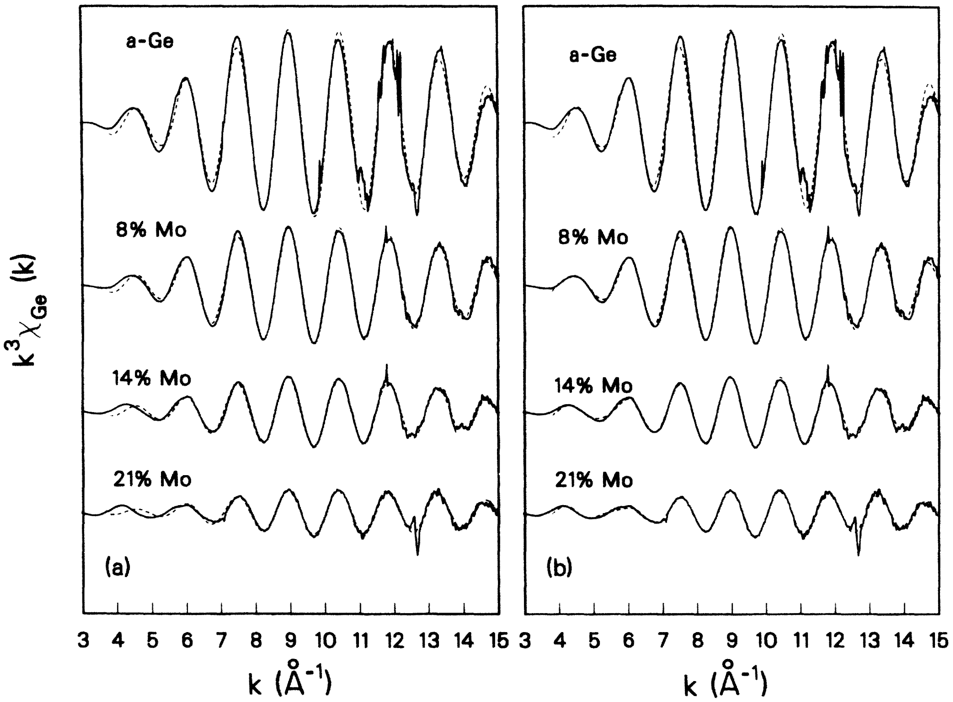

FIG. 9. Modeling results of the Ge $k^3\chi(k)$ with compositions <23 at. % Mo are shown here. (a) shows one-Ge-shell models superimposed on the data, and (b) shows two-shell models with one Ge and one Mo shell. Models are dashed curves, and data points are joined by solid lines. Modeling results are in Table IV.

ed amplitudes or in normalization. In general, the fits using the one-Ge-shell model are quite good for $k > 7$ Å^{-1} and become increasingly poor at lower k with increasing Mo content. Two-shell fits with Ge at the tetrahedral distance and Mo at a longer distance improve the fit at low k compared to the one-Ge-shell radius as seen in Fig. 9(b) and Table IV. For the 8-at. %-Mo sample, large N and σ^2 values for the Mo shell returned from the model are clearly unphysical, and show that the modeling technique can yield spurious results. For the 14- and 21-at. %-Mo samples, the Mo-shell parameters returned from the model are plausible, and show Ge-Mo distributions at roughly 2.61 Å with broader widths than the Ge-Ge first-shell distributions in *a*-Ge. We believe that these Ge-Mo distances reflect Ge-Mo correlations in the Mo-modified material that coexists with the *a*-Ge RTN at these compositions. Similar Ge-Mo distances are also observed in the Ge EXAFS in structural regions II and III and in the Mo EXAFS in regions I and II, as seen later.

For compositions above 23 at. % Mo, the modeling situation is much different. Here the data are better described by a Mo rather than a Ge one-shell model, as seen in Figs. 10(a) and 10(b) and Table V. For all compositions, the Ge-Mo model distance is about 2.58 Å while the Ge-Ge model distance is about 2.68 Å. No signs of tetrahedral *a*-Ge are present in this range, consistent with the scattering results. As seen in the figures and in the Σ values, the Mo one-shell model matches the data better than does the Ge one-shell model. Two-shell models with one Mo and one Ge shell improve the fit over the Mo one-shell results as seen in Fig. 10(c) and Table V. Improvement is most dramatic for the 42- and 65-at. %-Mo samples. In all cases, the one- and two-shell results are reasonably self-consistent, in the sense that two-shell best-fit results input into one-shell models lead to one-shell best-fit results, and vice versa. However, the Mo shell is more consistent between the one- and two-shell models, as seen in the more closely similar Ge-Mo than Ge-Ge distances in Table V. These results indicate Ge-Mo distances shorter and sharper than Ge-Ge distances over this composition range. Strongly increasing average coordination about Ge is indicated with increasing Mo composition, from a value at 23 at. % Mo which would appear to be even less than that for tetrahedral *a*-Ge.

These modeling results provide a picture of how the average environment about Ge changes with composition. As Mo is added to *a*-Ge, the EXAFS is primarily sensitive to what tetrahedral Ge remains, until about 23 at. % Mo, when all indications of tetrahedral Ge vanish. This is consistent with RDF and Ge DDF results. The Ge environment in this modified material evidently has Mo first neighbors in broad average shells (compared to the Ge-Ge shells in *a*-Ge) at longer distances. This situation, Ge surrounded most closely by Mo at about 2.58 Å, best describes the EXAFS over the entire range from 25 to 70 at. % Mo. The closest Ge-Ge distances in this range appear to be about 0.1 Å longer than the Ge-Mo distances, providing evidence for preferred Mo-Ge interaction, at covalentlike distances. The trends in total effective coordination number with composition in Tables IV and V suggest that the average Ge coordination first decreases and then increases with addition of

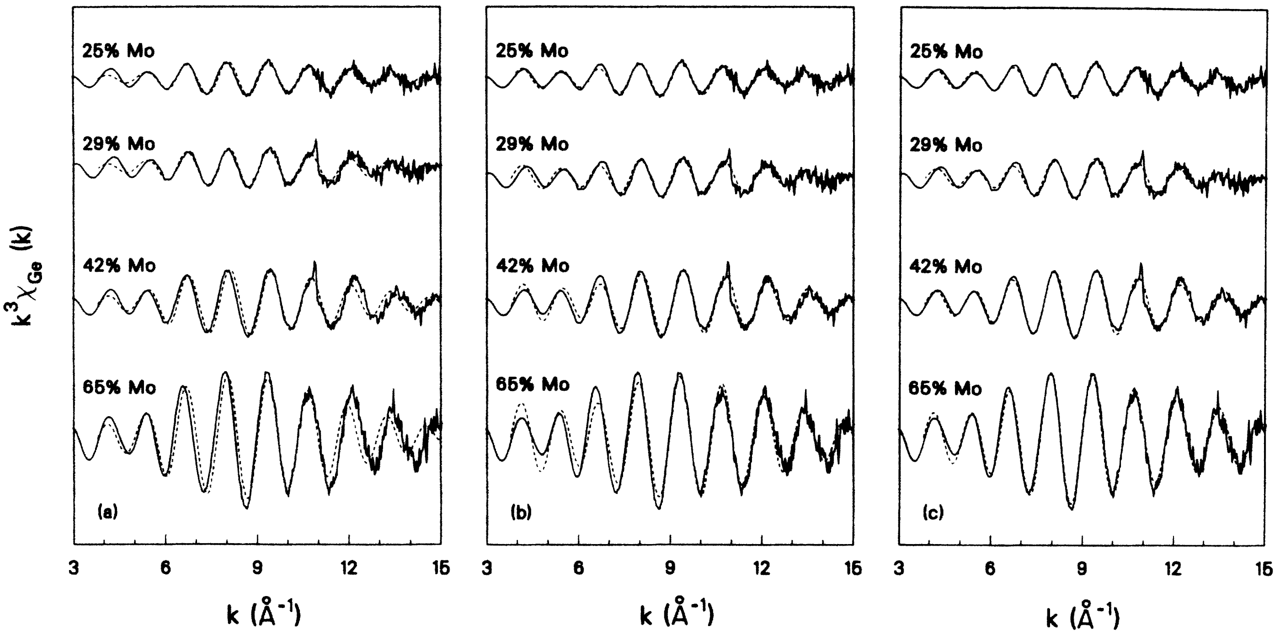

FIG. 10. Modeling results of the Ge $k^3\chi(k)$ with compositions >23 at. % Mo are shown here. (a) shows one-Mo-shell models, (b) shows one-Ge-shell models, and (c) shows two-shell models with a Mo and a Ge shell. Models are dashed curves, and data points are joined by solid lines. Modeling results are in Table V.

Mo. This curious behavior is not in agreement with scattering results. We believe that this low apparent coordination number at about 23 at. % Mo, and the trend with composition, are at least partly the result of extreme average structural disorder about Ge at 23 at. % Mo, as discussed in Sec. VI.

B. Mo EXAFS modeling results

$k^3\chi_{Mo}(k)$ from above the Mo edge for samples with compositions from 4 to 70 at. % Mo are in Fig. 11. The 4 at. % Mo data set is truncated at $k = 8.8$ Å^{-1} because of difficulties associated with obtaining a transmission EXAFS signal from a sample with such a low Mo concentration. Two distinct trends with composition are seen. For less than or equal to 42 at. % Mo, the EXAFS has a remarkably constant phase and a slowly decreasing amplitude with increasing Mo content, suggesting that the Mo nearest-neighbor environment is roughly constant in this range. At 65 and 70 at. % Mo the EXAFS has much reduced amplitude and a slightly different phase compared to that in the Ge-rich region. Unlike the case in the Ge EXAFS, where compositional division

TABLE V. Ge EXAFS modeling results ($\geq$ 25 at. % Mo). E_0 values used for these fit results correspond to the energy at the midpoint of the Ge edge rise. This E_0 was found to yield minimum Σ value for the Mo one-shell fit.

Mo conc.	Mo shell			Ge shell			
at. %	R	N	σ^2	R	N	σ^2	Σ
			Mo one-shell results				
25	2.59	1.03	0.0071				0.136
29	2.58	1.16	0.0070				0.157
42	2.57	1.75	0.0064				0.083
65	2.60	3.35	0.0063				0.095
			Ge one-shell results				
25				2.68	1.00	0.0064	0.204
29				2.68	1.14	0.0064	0.212
42				2.67	1.85	0.0064	0.179
65				2.70	3.73	0.0067	0.221
			Two-shell results				
25	2.59	0.64	0.0057	2.69	0.75	0.0140	0.128
29	2.57	0.76	0.0052	2.74	0.19	0.0020	0.145
42	2.56	0.75	0.0037	2.71	1.21	0.0080	0.056
65	2.58	1.60	0.0036	2.75	2.77	0.0088	0.042

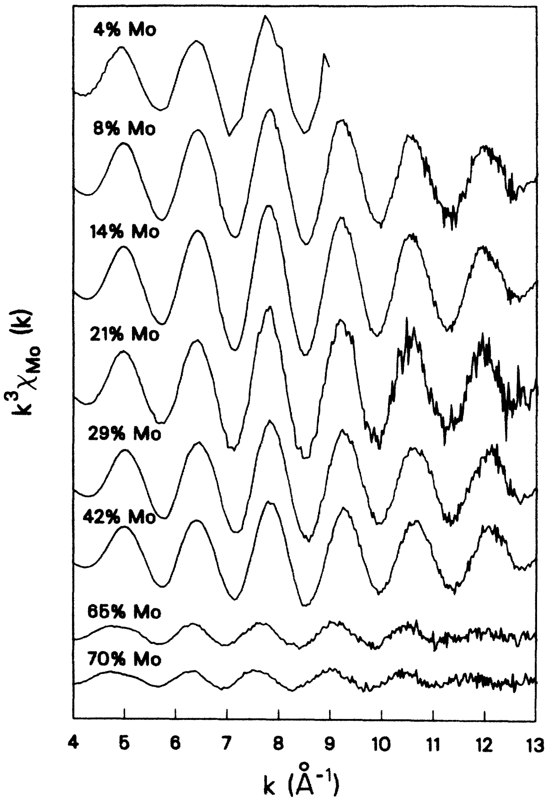

FIG. 11. Mo $k^3\chi(k)$ for a series of a-Mo-Ge samples with composition from 2 to 70 at. % Mo are shown here, all plotted on the same vertical scale and offset vertically for comparison.

between major trends occurs between regions I and II, in the Mo EXAFS the division occurs because regions II and III identified in the discussion of the scattering results. Modeling results for these two composition regions will be considered in turn.

In regions I and II, the Mo EXAFS is dominated by Ge neighbors at about 2.6 Å, as concluded from combined one- and two-shell modeling results summarized in Table VI. One-shell models with both a Ge and a Mo shell were investigated. The Ge one-shell fits have Ge at about 2.6 Å from the central Mo in a roughly constant number at less than about 21 at. % Mo and in a slightly decreasing number with increasing Mo content from there. The Mo one-shell fits have Mo at a very short 2.5 Å from the central Mo with similar composition trends. These Mo one-shell fits do not match the phase of the data across much of the k range and are not considered good fits. This is reflected in the much larger Σ values returned from the Mo one-shell fits compared to the Ge fits. Only the Ge shell of these one-shell models is consistent with two-shell models containing both a Ge and a Mo shell, as seen in the two-shell results which were obtained with the one-shell results as initial inputs to the two-shell model. The Ge-shell parameters are much more consistent between the one- and two-shell models than are the Mo-shell parameters, which show an increase in distance of 0.1 Å and unphysical σ^2 values for two compositions. In the two-shell models which do yield physically plausible parameters for the Mo shell, the improvement in the Σ value compared to that for the Ge one-shell fit is not consistent. These inconsisten-

TABLE VI. Mo EXAFS modeling results ($\leq$ 42 at. % Mo). The E_0 value used for these fits corresponds to the half-height of the Mo K edge jump.

Mo conc.	Ge shell			Mo shell			
(at. %)	R	N	σ^2	R	N	σ^2	Σ
			Ge one-shell results				
4	2.61	4.44	0.0085				0.053
8	2.60	4.36	0.0087				0.044
14	2.60	4.56	0.0082				0.023
21	2.61	4.16	0.0078				0.061
25	2.59	3.59	0.0081				0.043
29	2.59	3.37	0.0079				0.039
42	2.59	2.93	0.0077				0.047
			Mo one-shell results				
8				2.50	4.11	0.0092	0.146
14				2.51	4.21	0.0086	0.122
21				2.50	3.97	0.0083	0.144
25				2.49	3.26	0.0083	0.112
29				2.49	3.18	0.0083	0.104
42				2.49	2.71	0.0079	0.091
			Two-shell results				
8	2.58	3.71	0.0046	2.61	0.87	0.0047	0.040
14	2.59	4.18	0.0075	2.59	0.74	0.0065	0.020
21	2.60	3.87	0.0074	2.58	0.69	0.0072	0.059
25	2.60	3.97	0.0092	2.47	0.02	−0.0059	0.036
29	2.58	2.85	0.0068	2.58	0.78	0.0083	0.030
42	2.59	2.59	0.0106	2.48	0.11	−0.0014	0.030

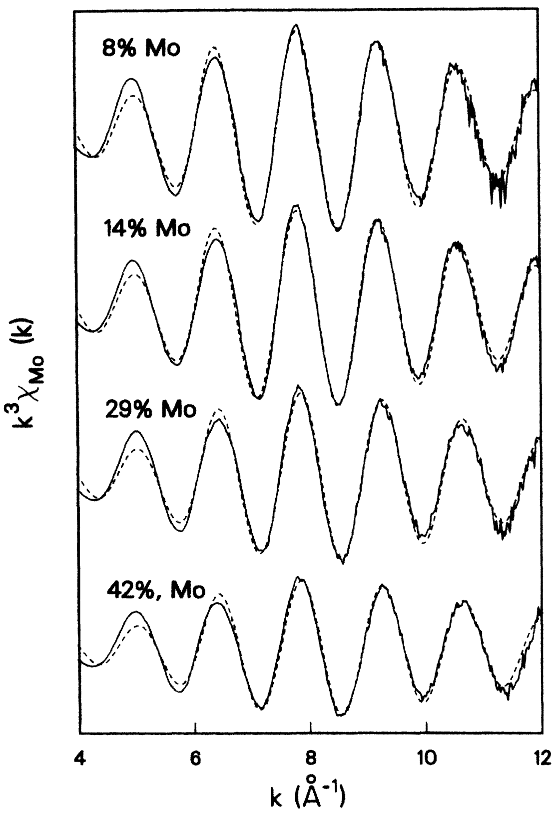

FIG. 12. One-Ge-shell modeling results of the Mo $k^3\chi(k)$ with compositions in regions I and II are superimposed on the data here. Models are dashed curves, and data points are joined by solid lines.

cies, together with the very poor Mo one-shell model compared to the Ge one-shell model, lead us to conclude that, within this simple two-shell model, only Ge at about 2.6 Å consistently accounts for the Mo EXAFS in this composition range. Figure 12 shows these Ge one-shell models superimposed on the data. The possibility of some Mo at roughly 2.6 Å cannot be ruled out, though this modeling study provides much stronger evidence for Mo-Ge neighbors than for Mo-Mo neighbors.

Modeling of the Mo EXAFS in region III is made difficult by the poor signal-to-noise level resulting from the decreased amplitude. This decreased amplitude is itself interesting, as a cursory interpretation may lead to the conclusion of decreased Mo coordination, which is inconsistent with scattering results, as discussed in the next section. Modeling results (Table VII) are similar to those just discussed for regions I and II. In a one-shell model, both a Ge and a Mo shell can fit the data, with the Ge shell at about 2.65 Å giving a slightly better fit than the Mo shell at a short 2.54 Å. When these one-shell results are input into a two-shell model as initial parameters of the fit, only the Ge shell yields a consistent result. The Ge one-shell fits are superimposed on the data in Fig. 13, and match the data fairly well above 6.0 Å^{-1}, but show significant deviations from the data at lower k, suggesting that broader shells might be contributing in that region.

Summarizing the Mo EXAFS with composition, these modeling studies suggest that Ge atoms at about 2.6 Å or slightly longer give the dominant contribution to the EXAFS over the entire composition range. This distance is much shorter than the sum of the metallic (Goldschmidt) radii, and suggests a strong preference for Mo to be surrounded by Ge at covalentlike distances. No contributions from Mo are consistently identified in the modeling. The constancy of Mo EXAFS from 4 to roughly 50 at. % Mo shows that the Mo environment of the Mo-modified material in region I is very similar to that in region II, where no tetrahedral Ge exists. This strongly suggests that Mo does not enter the a-Ge RTN in region I in a substitutional or interstitial fashion, but rather actively modifies the RTN to produce a preferred local structure like the average structure in region II. The slight decrease in amplitude with increasing Mo content in region II, and the sharp reduction in going to region III are not consistent with decreased coordination about Mo, when compared to DAS result, for reasons discussed in the next section.

From modeling the EXAFS with these simple Gaussian shell models we determine which species at what distances appear to make the primary contribution to the EXAFS at each edge. In most cases the data are relatively well fit by one- or perhaps two-shell models, with

TABLE VII. Mo EXAFS modeling results (≥ 65 at. % Mo). The E_0 value used for these fits corresponds to the half-height of the edge jump.

	Ge shell			Mo shell			
Mo conc. (at. %)	R (Å)	N	σ^2 (Å^2)	R (Å)	N	σ^2 (Å^2)	Σ
			Ge one-shell results				
65	2.64	0.88	0.0088				0.18
70	2.66	0.073	0.0095				0.21
			Mo one-shell results				
65				2.53	0.56	0.0064	0.25
70				2.55	0.49	0.0069	0.26
			Two-shell results				
65	2.63	0.80	0.0082	2.37	−3.58	0.062	0.11
70	2.67	1.03	0.014	2.52	0.03	−0.0028	0.19

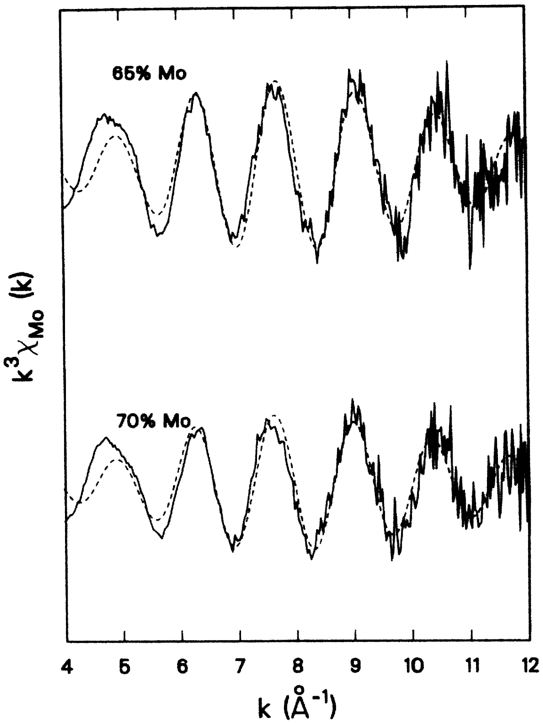

FIG. 13. One-Ge-shell modeling results of the Mo $k^3\chi(k)$ with compositions in region III are superimposed on the data here. Models are dashed curves, and data points are joined by solid lines.

the fits becoming less good at the lowest k values in some cases. The dominant contribution to the EXAFS at each edge across most of the composition range is from Mo-Ge neighbors at about 2.6 Å. At first glance some trends in the EXAFS results may appear inconsistent with those from the DAS technique. This is considered further in the next section.

VI. COMPARISON OF EXAFS AND SCATTERING RESULTS

Structural information has been obtained from EXAFS and scattering results in rather different ways. Scattering provides direct real-space results from interference oscillations in k space which have been normalized and transformed to r space with little ambiguity. We have chosen a less-direct modeling technique of the EXAFS data because of uncertainties in the choice of backscattering phases and amplitudes and other possible effects which make normalization to an absolute scale and transformation to unambiguous quantities in real space more difficult. Our choice of Gaussian shells for modeling the EXAFS is arbitrary. However, we are able to obtain relatively good fits based on these models. We feel this fitting procedure is justified because of the tendency of EXAFS oscillations to result from the sharpest, shortest, real-space features for disordered systems, as discussed more below.

DAS and EXAFS each provide information about the average environment of a single species in these a-Mo-Ge alloys. In comparing results from these different techniques applied to the same samples it must be remembered that each technique has a characteristic, and largely different, range of measurement in reciprocal space. The range of the DAS experiment is roughly $0.5 < k_{\text{scat}} < 10.5-15.0$ Å^{-1}, the upper limit depending on the x-ray wavelength. The effective k scale of EXAFS is twice that of scattering [because of the factor of 2 in the argument of the oscillatory term in Eq. (1)], so compared to scattering the EXAFS range is roughly $7.0 < 2k_{\text{EXAFS}} < 27.0$ Å^{-1}. Scattering measures interference oscillations in a range relatively near to the origin while EXAFS oscillations are not readily analyzed near the origin but rather in a higher region of reciprocal space. These largely different ranges, coupled with the large amount of average structural disorder about a given species in these amorphous alloys, result in largely different and complementary structural sensitivities.[19] These different sensitivities are reflected in the nature of the changes with composition of the k-space signals of the two techniques. The dominant changes in the $S(k)$'s and $\Delta[S(k)]$'s are in the shape of the lowest one or two interference oscillations which are largely below the EXAFS k range. The dominant changes in the $k^3\chi(k)$ are changes in phase between the structural regions identified and in amplitudes within structural regions. At the lowest k values, the $k^3\chi(k)$ show more subtle changes with composition.

Differences in structural information contained in the interference signals of the scattering and EXAFS techniques applied to amorphous solids are demonstrated in Fig. 14. Amorphous Ge is a good standard for comparison of the two techniques because of its relatively understood structure having a well-defined first shell consisting of four neighbors at a single, sharp, distance and less well-defined second and farther shells. In Fig. 14 are superimposed interference signals $S(k)$ and $k^3\chi(k)$ for scattering and EXAFS, respectively. The EXAFS k scale has been multiplied by 2, but the additional phase

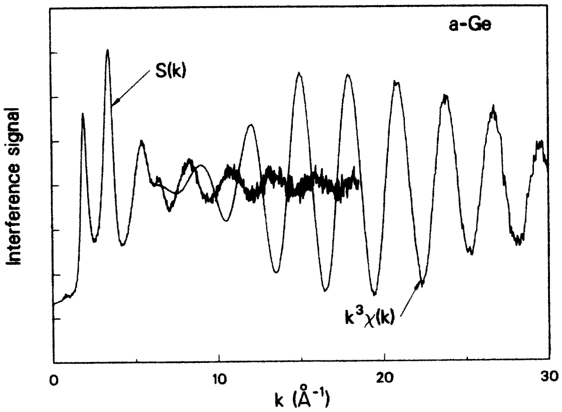

FIG. 14. Reciprocal-space oscillations from scattering and EXAFS are superimposed for amorphous Ge. The k scale of EXAFS has been multiplied by 2 for comparison with the scattering data, but EXAFS phase shifts have not been removed. In the region of overlap and at higher k, these interference oscillations result from only the sharp, first-neighbor distance.

shift has not been removed from the EXAFS data. In the region of overlap and at higher k the two signals both show the same single, low frequency. This lowest-frequency signal results from the first-neighbor distance, as demonstrated by the EXAFS modeling. The EXAFS data show no strong higher-frequency oscillations indicative of second and farther distances. The scattering signal, however, shows higher-frequency interference structure in the region closer to the origin, below the EXAFS range. Clearly this higher-frequency structure in $S(k)$ results from correlations beyond the first shell. Second and higher shells are evident in the RDF in Fig. 3. The increased average width, or static disorder, of these more-distant shells damps interference oscillations arising from these correlations[35] in the k range accessible to EXAFS. The results for a-Ge is that EXAFS and scattering each perceive the same first-neighbor structure, but only scattering measures well the damped interference signal from the farther neighbors.

Interference oscillations from average structural disorder in the first coordination shell can be damped so strongly with k that EXAFS is sensitive to only the sharpest or more well-defined features of the average first shell.[20,35,36,19,37] For the amorphous alloys we find that, just as the second and higher shells of a-Ge are perceived differently by EXAFS and scattering because they are disordered, so for the alloys even the first shells are perceived differently by the two tecnhiques. The EXAFS results indicate distances at the leading edge of the first shell compared to the DAS results for each species. The DDF's first-shell peak positions and widths increase significantly compared to a-Ge, and especially the Ge DDF's show poorly defined average coordination shells having many distances, on average, between the first and second shell. Evidently the sharpest structural features in each species' average environment is the distance of closest approach of the nearest neighbors in a broad first shell. EXAFS acts as a high-pass filter in k space to measure interference oscillations primarily from this sharpest feature. Scattering acts as a lower-pass filter, and real-space results place more emphasis on broader features in the average first and farther shells.

Having this understanding of the origin of the different structural sensitivities of EXAFS and scattering applied to these disordered alloys, we find that the techniques do give a consistent, although somewhat different, view of the changing amorphous structure as a function of composition. Both techniques consistently indicate similar divisions with composition between three structural regions. In region I both techniques are sensitive to some tetrahedral a-Ge and to some Mo-modified material. The transition between regions I and II is signaled by the disappearance of tetrahedral a-Ge in both techniques. The decreasing Ge EXAFS amplitude across region I might be interpreted as a decreasing average coordination about Ge, inconsistent with the increasing Ge coordination indicated by the Ge DDF at 14 at. % Mo. Instead, we interpret the Ge EXAFS as dominated by the remaining tetrahedral Ge and infer that the Ge associated with the Mo-modified material is very disordered, on average, so that its EXAFS is strongly damped. Indeed, significant disorder about the Mo-modified Ge in region I is seen in the Ge DDF at 14 at. % Mo. Both techniques indicate that the Mo environment in the Mo-modified material in region I is dominated by Ge nearest neighbors, and the Mo DDF shows Mo-Mo distance at about 3.3 Å, to which the Mo EXAFS is not sensitive. The Ge EXAFS more precisely shows the composition delimiting regions I and II is between 21 and 25 at. % Mo, with no data for intermediate compositions. Composition trends in both DAS and EXAFS show that the average structure in region II is much like the Mo-modified material in region I. This disorder is also evident in the crystalline compounds Ge_2Mo and $Mo_{13}Ge_{23}$, as discussed in Sec. IV B.

Both techniques consistently indicate that Mo-Ge distances are the shortest in region II. The DDF's show that in addition to Mo-Ge nearest neighbors, the Ge environment is characterized by extremely disordered Ge-Ge distances extending between the first and second shells and the Mo environment by long Mo-Mo distances at about 3.3 Å. Likewise both techniques show that the Mo average environment shows the dominant change with composition on going to the Mo-rich alloys, signaling the transition between regions II and III. Both techniques show that only small changes occur in the Ge average environment between regions II and III. The Mo DDF's show that the long Mo-Mo first distances of regions I and II collapse on going to region III into a very broad and large first shell. The Mo EXAFS shows a drastic reduction in amplitude on this transition, which is interpreted as indicating a very disordered average first shell about Mo rather than a decreased coordination number. Strong chemical ordering of Mo about Ge at the shortest distances is consistent with both techniques at 65 at. % Mo.

The potential of EXAFS to miss structural information from even the first average coordination shells is a serious limitation of this technique applied to structurally disordered materials. However, just as EXAFS acts as a high-pass filter in reciprocal space, thus missing oscillations from highly disordered features, so scattering acts as a low-pass filter and is less sensitive to the sharpest features. The two techniques are thus complementary, and both should be applied to the study of disordered structures when possible.

VII. SUMMARY AND CONCLUSIONS

The combined techniques of small-angle x-ray scattering, large-angle x-ray scattering (including anomalous scattering), and EXAFS yield a complementary, consistent, and very detailed description of changing atomic-scale structure with composition in sputtered amorphous Mo-Ge alloys across the range from 0 to 65 at. % Mo. Normalized small-angle scattering allows limits to be set on compositional inhomogeneity, and trends in the SAS intensity with composition, together with information from other techniques, are meaningful in interpreting the nature of the inhomogeneity. Large-angle scattering provides structural information about short- and intermediate-range order in these materials, and differential anomalous scattering provides chemical-specific information on these size scales. EXAFS, because of its lack of low-*k* data together with the large amount of structural disorder even in the first shells of the amorphous alloys, provides direct chemical-specific information about the sharpest distance distributions in the average first shells of these, as well as indirect information about the amount of disorder on average about a given species from trends with composition and comparison with scattering data.

Three structural regions are distinguished as a function of composition. Major changes in the average environment of one species or the other delimit these structural regions, though structural changes with composition also occur within the regions.

We emphasize that the three structural regions identified in this work are simply a means of classifying the major structural changes with composition. Physical properties are not necessarily expected to show major changes at the compositions delimiting the structural regions. For example, the semiconductor-metal transition is expected to occur somewhere near the middle of structural region I, rather than between regions I and II, based on this structural study.

Structural region I extends from amorphous Ge to about 23 at.% Mo. As Mo is added to tetrahedral *a*-Ge on the 1 at.% level and above, it does not substitute for Ge in the RTN or occupy interstitial-like sites in the RTN. Rather, Mo atoms appear to actively modify the tetrahedral Ge to yield local structures much like those in the Ge-rich intermetallic compounds. The Mo-modified material has a distinct local structure characterized in part by Mo atoms highly coordinated by Ge with the closest Ge at short, covalentlike distances. This Mo-modified material coexists with the remaining tetrahedral *a*-Ge and modifies more of the Ge with increasing Mo content. This coexistence of two distinct local structures occurs on a very fine size scale, and is not well described as phase separation, except perhaps in its incipient stages. A peak in the diffuse SAS intensity at 8 at.% Mo suggests that near this composition the two local structures exist in some sense in equal amounts, with the tetrahedral *a*-Ge decreasing as it is modified by Mo with increasing Mo content. By 14 at.% Mo, Mo-Mo neighbors are seen at distances (3.3 Å) longer than the Mo-Ge distances, indicating some segregation of Mo-modified regions. The Mo-modified material is also characterized by extremely disordered Ge-Ge correlations and, above 14 at.% Mo at least, by long Mo-Mo first distances which increase in number as the modified material consumes the remaining RTN. All indications of amorphous Ge with tetrahedral character vanish at roughly 23 at.% Mo. EXAFS shows that the Mo first-nearest-neighbor environment remains remarkably constant as Mo modifies the *a*-Ge, and that at 23 at.% Mo the Ge average environment shows a maximum of disorder. From these structural data the transition from semiconductor to metal is expected to occur somewhere toward the middle of structural region I, as observed in work by Yoshizumi *et al.*[13] The compositional inhomogeneity towards the middle of region I, resulting from a finely dispersed mixture of tetrahedral *a*-Ge and Mo-modified material, is equaled at no other composition. This changing amorphous structure with composition through the semiconductor-metal transition has important implications for the physical mechanisms giving rise to this transition which are beyond the scope of this work.

Structural region II extends from 23 at.% Mo to roughly 50 at.% Mo. Changes in the average structure with composition are much less dramatic in region II than in region I. The average structure in region II is characterized by Mo-Ge correlations shortest, Ge-Ge correlations very disordered, and rather long Mo-Mo first distances. These correlations are extremely similar to those in the intermetallic compounds Ge_2Mo and $Mo_{13}Ge_{23}$, and also to those in the Mo-modified material of region I. It appears that specific chemical interaction between Mo and Ge similar to that in these compounds accounts for the local structures in the amorphous alloys in region II. The average structure is not well described as a dense random packing of two-size spheres in region II. RDF's and EXAFS show the average structure changes little with composition from 23 to roughly 50 at.% Mo. Those structural changes that do take place appear to accommodate the specific interaction between Mo and Ge so that the characteristic correlations mentioned above remain largely intact. The increasing amplitude of the Ge EXAFS with Mo content suggests that the average Ge environment becomes more well defined, while the decreasing Mo EXAFS amplitude suggests that its average first-neighbor environment becomes more disordered.

Structural region III is the Mo-rich material, and the composition delimiting regions II and III is poorly defined due to the lack of data between these regions. In region III the structure was studied only at 65 at.% Mo, where the RDF and especially the Mo DDF look much like RDF's of typical melt-quenched transition-metal–metalloid glasses. The major structural change delimiting regions II and III is the collapse of the long Mo-Mo distances from about 3.3 Å in region II to shorter distances still longer than the Mo-Ge neighbors in region III. This shortening of Mo-Mo first-nearest-neighbor distances represents the partial breakdown of the chemical ordering of the Mo-modified material of region I and the average structure of region II, and can be thought of as a natural consequence of the increased Mo concentration. The Ge average environment changes little between regions II and III, indicating a strong preference for Mo-Ge nearest neighbors.

ACKNOWLEDGMENTS

The authors acknowledge P. H. Fuoss for laying experimental groundwork for the DAS technique and for data-analysis programs, and G. B. Stephenson for SAS equipment and analysis programs. Many aided in data collection: W. K. Warburton, S. Laderman, A. Fischer-

Colbrie, K. Ludwig, and D. Lorentz. TEM results cited were obtained by A. Marshall. This work was supported by the NSF-sponsored Thrust Program in Metastable Materials in the Center for Materials Research at Stanford University and by SSRL which is supported by the Department of Energy, Office of Basic Energy Sciences, and the National Institutes of Health, Biotechnology Resource Program, Division of Research Resources.

---

*Present address: Center for X-ray Optics, Lawrence Berkeley Laboratory, University of California, Berkeley, California 94720.

[1] D. E. Polk, J. Non-Cryst. Solids **5**, 365 (1971).
[2] D. E. Polk, Scr. Met. **4**, 117 (1970).
[3] J. D. Bernal, Nature **183**, 141 (1959); **185**, 68 (1960).
[4] D. E. Polk, Acta Met. **20**, 485 (1972).
[5] H. S. Chen and B. K. Park, Acta Met. **21**, 395 (1973).
[6] J. W. Allen, A. C. Wright, and G. A. N. Connell, J. Non-Cryst. Solids **42**, 509 (1980).
[7] F. A. Shunk, *Constitution of Binary Alloys, Second Supplement* (McGraw-Hill, New York, 1969), p. 388.
[8] W. L. Johnson, C. C. Tsuei, S. I. Raider, and R. B. Laibowitz, J. Appl. Phys. **50**, 4240 (1979).
[9] S. Ikeda, H. Fujimori, M. Idebe, Y. Muto, and K. Suzuki, in *Proceedings of the Fourth International Conference on Rapidly Quenched Metals, Sendai, Japan, 1981,* edited by T. Matsamoto and K. Suzuki (Japan Institute of Metals, Sendai, 1982), p. 1253.
[10] G. S. Brown, L. R. Testardi, J. R. Wernick, A. B. Hallak, and T. H. Geballe, Solid State Commun. **23**, 875 (1977).
[11] H. Daver, O. Massenet, and B. K. Chakraverty, Solid State Commun. **11**, 131 (1972).
[12] K. Kobayashi, F. Itoh, T. Fukunaga, H. Fujimori, and K. Suzuki, in *Proceedings of the Fourth International Conference on Rapidly Quenched Metals, Sendai, Japan,* Ref. 9, p. 376.
[13] S. Yoshizumi, D. Mael, T. H. Geballe, and R. L. Greene, in *Localization and Metal Insulator Transitions,* edited by H. Fritzsche and D. Adler (Plenum, New York, 1985), p. 73.
[14] H. S. Randhawa, P. Nath, L. K. Malhotra and K. L. Chopra, Solid State Commun. **20**, 73 (1976).
[15] K. Yamada, Y. Endoh, Y. Ishikawa, and N. Watanabe, J. Phys. Soc. Jpn. **48**, 992 (1980).
[16] A. Devenyi, A. C. Rusu, A. Belu, and R. Manaila, J. Phys. (Paris) Colloq. **4**, C-1089 (1981).
[17] A. S. Nowick and S. Mader, IBM J. Res. **9**, 358 (1965).
[18] P. H. Fuoss, P. Eisenberger, W. K. Warburton, and A. Bienenstock, Phys. Rev. Lett. **46**, 1537 (1981); P. H. Fuoss, Ph.D. thesis, Stanford University, 1980 [Stanford Synchrotron Radiation Report No. 80/06 (unpublished)].
[19] J. B. Kortright, W. K. Warburton, and A. Bienenstock, in *EXAFS and Near Edge Structure,* edited by A. Biancone, L. Incoccia, and S. Stipcich (Springer-Verlag, Berlin, 1983), p. 362.
[20] P. Eisenberger and G. S. Brown, Solid State Commun. **29**, 481 (1979).
[21] T. W. Barbee and D. L. Keith, in *Synthesis and Properties of Metastable Phases,* edited by E. S. Machin and T. J. Rowland (AIME, New York, 1980), p. 93.
[22] A. F. Marshall (private communication).
[23] G. B. Stephenson, Ph.D. thesis, Stanford University, 1982 [Stanford Synchrotron Radiation Laboratory Report No. 82/05 (unpublished)].
[24] J. B. Kortright, Ph.D. thesis, Stanford University, 1984 [Stanford Synchrotron Radiation Laboratory Report No. 84/05 (unpublished)].
[25] A. Guinier and G. Fournet, *Small-angle Scattering of X-rays* (Wiley, New York, 1955).
[26] D. T. Cromer and J. B. Mann, Acta Crystallogr. Sect. A **42**, 321 (1968).
[27] W. H. McMaster, N. Kerr Del Grande, J. H. Mallett, and J. H. Hubbell, *Compilation of X-ray Cross Sections* (NTIS, Springfield, VA, 1969).
[28] J. J. Hoyt, D. DeFontaine, and W. K. Warburton, J. Appl. Cryst. **17**, 344 (1984).
[29] D. T. Cromer and D. A. Liberman, Acta Crystallogr. Sect. A **37**, 267 (1981); J. Chem. Phys. **53**, 1891 (1970).
[30] B. E. Warren, *X-ray Diffraction* (Addison-Wesley, Reading, Mass., 1969), Chap. 10.
[31] G. S. Cargill III, in *Solid State Physics,* edited by H. Ehrenreich, F. Seitz, and D. Turnbull (Academic, New York, 1975), Vol. 30, p. 227.
[32] B. K. Teo and P. A. Lee, J. Am. Chem. Soc. **101**, 2815 (1979).
[33] N. Alberding and E. D. Crozier, Phys. Rev. B **27**, 3374 (1983).
[34] B. K. Teo, J. Am. Chem. Soc. **103**, 3990 (1981).
[35] S. H. Hunter, A. Bienenstock, and T. M. Hayes, in *The Structure of Non-Crystalline Materials,* edited by P. H. Gaskell (Taylor and Francis, London, 1977), p. 73.
[36] M.-L. Theye, A. Gheorghin, and H. Launois, J. Phys. C **13**, 6569 (1980).
[37] G. S. Cargill III, W. Weber, and R. F. Boehme, in *EXAFS and Near Edge Structure,* edited by A. Bianconi, L. Incoccia, and S. Stipchich (Springer-Verlag, Berlin, 1983), p. 277.